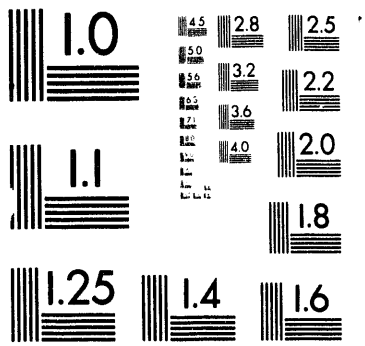
1.0
1.1
1.25
1.4
1.6
1.8
2.0
2.2
2.5
2.8
3.2
3.6
4.0
4.5
5.0
5.6

1 of 1

SIMULATION OF THE INDIAN AND EAST-ASIAN SUMMER MONSOON IN THE ECMWF MODEL: SENSITIVITY TO HORIZONTAL RESOLUTION

Kenneth R. Sperber[1], Sultan Hameed[2], Gerald L. Potter[1]
and
James S. Boyle[1]

[1]Program for Climate Model Diagnosis and Intercomparison
Lawrence Livermore National Laboratory
P. O. Box 808, L-264
Livermore, CA 94551

[2]Institute for Terrestrial and Planetary Atmospheres
State University of New York
Stony Brook, NY 11794-5000

November 1993

ABSTRACT

The ability of the ECMWF model (Cycle 33) to simulate the Indian and East Asian summer monsoon is evaluated at four different horizontal resolutions: T21, T42, T63, and T106. Generally, with respect to the large scale features of the circulation, the largest differences among the simulations occur at T42 relative to T21. However, on regional scales, important differences among the high frequency temporal variability serve as a further critical test of the model's ability to simulate the monsoon. More generally, the results indicate the importance of evaluating high frequency time scales as a component of the climate system.

T106 best captures both the spatial and temporal characteristics of the Indian and East Asian Monsoon, while T42 fails to correctly simulate the sequence and development of synoptic scale milestones that characterize the monsoon flow. In particular, T106 is superior at simulating the development and migration of the monsoon trough over the Bay of Bengal. In the T42 simulation, the development of the monsoon occurs one month earlier than typically observed. At this time the trough is incorrectly located adjacent to the east coast of India which results in an underestimate of precipitation over the Burma/Thailand region. This early establishment of the monsoon trough affects the evolution of the East-Asian monsoon and yields excessive preseason rainfall over the Mei-yu region. EOF analysis of precipitation over China indicates that T106 best simulates the Mei-yu mode of variability associated with an oscillation of the rainband that gives rise to periods of enhanced rainfall over the Yangtze River Valley. The coarse resolution of T21 precludes simulation of the aforementioned regional scale monsoon flows.

1. Introduction

In order to evaluate the consequences of climate change for agriculture and the economy, we need to develop climate models capable of simulating regional precipitation patterns with a high degree of fidelity. The deficiency of global climate models in the simulation of orographic precipitation may be related to the crudeness of model topography. Inadequacies in the parameterizations of physical processes cause additional errors in the calculation of orographic as well as frontal precipitation. In this study, we investigate the role of model resolution in simulating the geographical distribution of precipitation over India and China during the summer monsoon.

Simulation of the Indian monsoon has proven to be a critical test of a general circulation models ability to simulate tropical variability (WCRP 1992, 1993). These studies, performed under the guidance of the Monsoon Numerical Experimentation Group (MONEG), have generally concentrated on monthly and seasonal time scales. In this study, we will pay particular attention to the evolution of monsoon circulation patterns using daily data from annual cycle simulations of Cycle 33 of the ECMWF model carried out at horizontal resolutions of T21, T42, T63, and T106. Our purpose is to evaluate high frequency variations, the ensemble of which determine climate, since it is important to determine if the synoptic scale physical and dynamical processes are correctly represented, otherwise prediction of regional climate change will be suspect. In this vein, Slingo et al. (1992a) and Slingo et al. (1993) reported on the sensitivity of synoptic scale aspects of the monsoon circulation to two different convective parameterizations utilized in the UGAMP GCM. While each of these simulations gave rise to similar climatologies, the transient characteristics of the tropical variability were vastly different, thus demonstrating the difficulty of parameterizing subgrid scale processes.

In an effort to validate the simulation of tropical variability on intradiurnal and interdiurnal time scales, Slingo et al. (1992b) employed the T106 ECMWF Cycle 33 model used in this study in perpetual January and July simulations. They demonstrated the fidelity of this model in simulating easterly waves with well defined periodicities during July. Specifically, the model produced African easterly waves with a preferred time scale of 3.5 days and their lower frequency counterpart with a period of 6 days that originate in the eastern Pacific near South America. During January, the model tended to produce variations in the frequency range associated with in-

traseasonal oscillations. We are currently evaluating these features in the resolution runs described in this paper to determine the sensitivity of the tropical transience to horizontal resolution. This work will be presented in a forthcoming report.

To date, resolution studies have generally evaluated the time mean aspects of the large-scale circulation (Hansen et al. 1983, Boer and Lazare 1988, Tibaldi et al. 1990, Boville 1991, Kiehl and Williamson 1991, Boyle 1992, Gleckler and Taylor 1993, Phillips et al. 1994). In this paper, after reporting on some large-scale features, we also include an evaluation of regional characteristics derived from daily data. Since a major improvement in the high resolution models is the more detailed topography, we may expect significant differences between models in areas where atmospheric flows interact with topographic features. Simulation of the monsoon is of particular interest because of the role of the Tibetan Plateau in influencing the patterns of monsoon rainfall. In the previous resolution studies, monsoon simulation has only been addressed by Tibaldi et al. (1990). They analyzed monthly mean data from a series of 30-day integrations and concluded that large-scale features of rainfall were not significantly improved at resolutions higher than T42, but the T63 and T106 simulations showed more small-scale features of the rainfall distribution. They concluded that, with regard to the low-level circulation, T42 was adequate for climate simulations. However, Tibaldi et al. (1990) made no reference to the sensitivity of synoptic scale phenomena to horizontal resolution.

In the present study, several shortcomings exist in the context of annual cycle simulations of limited duration. We have extended the T42 simulation to two annual cycles in an attempt to address the effect of internal variability that may give rise to unforced interannual variations. Given that the SST's were repeated in the second year, it has been found in studies with these simulations that the differences of seasonal mean and annual means between the two years were generally smaller than the differences between the various resolutions (Gleckler and Taylor 1993, Phillips et al. 1994). Additionally, work under the auspices of MONEG has revealed that simulation of the Indian monsoon rainfall is sensitive to the initial conditions, more so than that of the Sahel region (WCRP 1992, 1993). Each of the simulations reported here used the same initial conditions (truncated from T106 to the appropriate resolution), hence, generating a set of internally consistent simulations whose differences may not be ascribed to marked differences in the large-scale structure of the initial state.

In the future, we expect to explore the sensitivity of the Indian and East Asian monsoons to interannually varying SST through analysis of models participating in the Atmospheric Model Intercomparison Project (Gates, 1992). Within AMIP, a suite of T42 ECMWF Cycle 36 simulations are being performed using different initial conditions, as well as one T106 Cycle 36 run of the latter portion of the AMIP decade. Additionally, one T42 Cycle 33 AMIP simulation and a complementary T106 Cycle 33 simulation will be completed. These simulations will provide a comprehensive test bed of the conclusions developed in this paper from a much more restricted set of integrations.

2. The Model

In this study we utilize the Cycle 33 forecast model of the European Centre for Medium-Range Weather Forecasts. This model, operational during late 1989, was integrated through 1 annual cycle (2 annual cycles at T42) at each of four horizontal resolutions, T106, T63, T42, and T21. These simulations use the monthly mean climatological sea-surface temperatures (SST) of Alexander and Mobley (1976). The SST was updated daily via linear interpolation. Descriptions of the dynamical and physical parameterizations of the model are found in Simmons et al. (1988) and Tiedtke et al. (1988), respectively. The model has 19 levels in the vertical, represented by a hybrid coordinate.

Important features of this version of the model that differ from those described in Tiedtke et al. (1988) include the convective and radiative parameterizations. Convective processes are parameterized using the mass flux scheme developed by Tiedtke (1989). The scheme represents various types of convection, from the penetrative convection maintained by large-scale convergence of moisture to the shallow convection such as tradewind cumuli, associated with suppressed conditions. The radiation parameterization is described in Morcrette (1990, 1991); its correction of known errors in the shortwave and longwave clear sky heating profiles give much greater destabilization of the tropical atmosphere and, consequently, a much more vigorous hydrological cycle. The radiative properties of clouds were also modified such that the emissivities of tropical cirrus clouds were increased, resulting in a much improved simulation of the outgoing longwave radiation (Morcrette 1990). These afore-mentioned parameterizations, in addition to the surface scheme of Blondin and Böttger

(1987) differ from those employed in the Tibaldi et al. (1990) resolution study with Cycle 28 of the ECMWF forecast model.

The model includes a diurnal cycle, with full radiation calculations being performed every 3 hours. In the intervening time, the radiation fields are updated every time step using the instantaneous solar zenith angle in the shortwave and the instantaneous temperature profile in the longwave. The operational version of the ECMWF model performs the full radiation calculations on a reduced horizontal grid in order to limit the computation time. In the present integrations, however, the full radiation calculation is performed at every grid point.

Consistent with the Tibaldi et al. (1990) study, the biharmonic horizontal diffusion coefficients in the T106 simulation were reduced by a factor of two from those used in the T21-T63 simulations. This modification was the only change made to the model physics as the resolution was increased from T21 to T106. All of the simulations employ the gravity wave drag (GWD) parameterization of Palmer et al. (1986), unlike the Boyle (1992) resolution study in which the GWD scheme was turned off in the T21 simulation since it gave rise to an unstable integration. A reduction of the numerical time step used for the T21 simulation (J.-J. Morcrette and D. Stephenson, personal communication) gave rise to a stable integration, which is utilized in this paper and in the resolution studies by Gleckler and Taylor (1993) and Phillips et al. (1994).

3. Indian Monsoon: June/July/August Means

a. Precipitation

Figure 1 shows the June/July/August (JJA) average precipitation rate for the four resolution runs, and, the Legates and Willmott (1990) and Jaeger (1976) climatologies. Over India, T21 (Fig. 1d) is unable to resolve the sharp decrease in precipitation to the east of the western Ghats, the rainshadow effect in the lee of the mountains simulated in the higher resolutions and seen in the observations. T21 calculates a region of low precipitation over the Bay of Bengal in contradiction to the observed pattern. T42-T106 give more realistic simulations over this region, in addition to more details of the rainfall distribution around the Himalayas. A significant systematic bias in the T42-T106 simulations is the excessive precipitation over the southern tropics of the Indian Ocean and underestimation just to the north. This

structure is associated with a systematic error in the zonal mean (60°E-115°E) vertical velocity, shown for T106 in Fig. 2. On a climatological basis, the ascending and descending branches of the Hadley cell are observed to be located near 15°N and 25°S respectively (Newell et al. 1972). In T42-T106 the Hadley cell has expanded poleward, with incorrectly simulated upward vertical velocities exceeding 0.1Pa s^{-1} associated with the region of incorrectly simulated precipitation. It is this region of erroneous ascent that dominates the poor mean meridional circulation profiles for the T42-T106 simulations as given in Boyle (1992). The associated upper level outflow and subsidence north of the equator coincides with the region of underestimated precipitation over the Indian Ocean seen in T42-T106. Later versions of the model, beginning with Cycle 36, incorporate a modification that enhances the heat and moisture transfer coefficients under low wind speed conditions and reduce these systematic errors (Miller et al. 1992). With regard to the influence of the low-level circulation, Tibaldi et al. (1990) reported a systematic northward displacement of the precipitation maximum along the west coast of India, which resulted from displacement of the 850hPa flow over the Arabian Sea. Although this model has a similar bias in the low-level flow, as will be discussed in a Section 3c, a displacement of the coastal precipitation maximum is not as readily apparent.

b. 200hPa velocity potential

The velocity potential is a gross measure of the global scale divergent and convergent centers of action. The 200hPa velocity potential generally has a wave number 1 structure with divergence located over the eastern hemisphere near Indonesia and convergence over the Atlantic Ocean. The divergent center is usually located coincident with the warmest SSTs in the tropical western Pacific, and migrates between the Philippines and Australia as the season progresses from the boreal to austral monsoon.

Figure 3 shows the simulated and analyzed JJA 200 hPa velocity potential fields. Only the T21 simulation captures the wave number 1 structure of the upper level divergent flow. The center in the eastern hemisphere is systematically displaced to the west of the analyzed local over the western Pacific warm pool. The T21 version produces divergent and convergent centers of action that are more intense than those of the analyses, whereas in T42-T106 contain a consistent pattern with slightly weaker

divergent flow over the eastern hemisphere. The T106 simulation displays the smallest error over the eastern hemisphere. These results are contrary to Tibaldi et al. (1990), who found the systematic underestimation of the divergent flow to increase from T21 to T106 in averages of 30-day integrations for the period April to September. At the higher resolutions the dominant divergent center occurs over the eastern Pacific near 100°W, 10°N, a feature not found in the Tibaldi et al. (1990) simulations nor in the observations. Boyle (1992) demonstrated that this anomalous convection center adjacent to the Central American coast has little effect upon the stationary wave structure of the model given that the associated Rossby wave source does not extend beyond the tropical easterlies; hence the waves die out locally.

c. 850 hPa winds

The July (rather than JJA in order to facilitate comparison with the resolution study of Tibaldi et al. 1990) wind field at 850 hPa, Fig. 4, shows the low-level cross-equatorial flow and the Somali Jet that characterize the monsoon circulation. To the east of 60°E over the Arabian Sea, the Somali Jet is displaced northward of the analyzed fields. Thus, the onshore flow is too strong over northwestern India and too weak over the southern coast. This was also noted in the 30-day simulations reported in Tibaldi et al. (1991) and the 90-day simulation by Miller et al. (1992) using a version of the ECMWF model without the low wind speed moisture and heat transfer coefficient modification. The maximum velocity at the core of the Somali Jet is observed to be approximately 15-20 m s^{-1}, as seen in Figs.4e and 4f. Relative to the observations, T106 and T21 best simulate this feature of the monsoon circulation. The resolution dependence of the strength of the core of the Somali Jet is inconsistent with that found in Tibaldi et al. (1990), in which the jet weakened progressively with higher resolution. In the present simulations however, T106 improves relative to the weak jet found in T42 and T63. Additionally, T42 and T63 underestimate the windspeeds over the northern equatorial Indian Ocean to a greater extent than T106. This is consistent with the rainfall rates of <1mm day^{-1} in this region simulated by T42 and T63, while precipitation rates of 1-2mm day^{-1} are produced by T106. The low windspeeds preclude the moisture flux convergence necessary to drive the convection scheme and result in the reduced precipitation.

It must be reiterated that major changes to the physics package have been made since the Tibaldi et al. (1990) study. These include, but are not limited to, replacement of the modified Kuo convection scheme with the Tiedtke (1989) mass flux scheme, revised radiation, a modified gravity wave drag scheme, and a new parameterization of land surface processes and vegetation. It is therefore difficult to determine the cause of the differing resolution dependences between Tibaldi et al. (1990) and this current investigation. However, these changes to the model have led to improvements in the afore-mentioned aspects of monsoon simulation, particularly at higher resolutions.

4. Indian Monsoon Evolution: Synoptic Time Scales

a. Overview

The Indian monsoon may be characterized in terms of onset and withdrawal phases. The onset, defined as persistent rainfall over the southwest subcontinent, occurs near June 1 although the date may vary between mid-May and mid-June (Das, 1984). The monsoon trough over the Bay of Bengal moves progressively northward and by mid-July the rains reach most of the Indian subcontinent and last until early September. Then the withdrawal begins from north to south, with the last vestige of monsoon rainfall occurring over the southern tip of India in early October. Figure 5 shows the temporal evolution of the Indian monsoon given by the average daily precipitation rate of all land points over the subcontinent south of 25°N. There is persistent rainfall prior to the normal time of onset, particularly in the lower resolution simulations. The intensification of the monsoon precipitation over the Indian subcontinent during late May and early June is preceded by the buildup of rotational kinetic energy at 850 hPa (not shown) is similar to that observed by Krishnamurti and Ramanathan (1982).

A major component of monsoon development is the northward propagation of the convergence zone over the Bay of Bengal. Observations indicate that disturbances propagate from near 5°N to approximately 25°N several times during the monsoon season, as shown in precipitation near 90°E (Fig. 4 of Gadgil and Srinivasan 1990) and ECMWF analyses of positive relative vorticity over the western Bay of Bengal (Fig. 6 of Slingo et al. 1992a). Time latitude diagrams of relative vorticity and precipitation for these locations are given for T106 and T42 in Fig. 6. In T42, Fig. 6c, the

magnitude of the relative vorticity in underestimated in comparison with the ECMWF analyses (Slingo et al. 1992a), and northward propagation is not evident. The associated precipitation, Fig. 6d, also develops in place unlike that observed (Gadgil and Srinivasan 1990). The magnitude of the T106 relative vorticity and its propagation characteristics, Fig. 6a, are more similar to the observations than T42, although clear progression from 5°N is not as readily apparent. In T106 the two episodes of northward movement of cyclonic vorticity occurring about June 10 and July 10 are associated with the enhanced precipitation episodes (Fig. 6b). These correspond to the June and July maxima in the subcontinental monsoon precipitation index in the T106 simulation shown in Fig. 5a.

These results suggest that T106 is superior to T42 in simulating regional scale temporal characteristics of the Indian monsoon. Further evidence of the benefit of using high horizontal resolution can be found from examination of the models ability to simulate the phenomenological evolution of the Indian/East Asian monsoon as characterized by Luo and Yanai (1983). They used pentad averages of observed 850hPa winds and precipitation from the FGGE Level II-b data set obtained during the Summer MONEX of 1979. Although the Luo and Yanai (1983) data only cover the period late May through early July, the significant milestones in monsoon development that they present are robust features that generally recur yearly. Similar features are found in Asian summer monsoon circulation statistics for the period 1979-84 based upon ECMWF analyses (Mohanty et al. 1985). We will investigate how well the models simulate these observed dynamical structures which characterize the development of significant milestones in the evolution of the monsoon. Since these features generally occur during the course of the monsoon development during any given year, the comparison between the simulations and observations is made irrespective of a one to one correspondence with respect to the precise timing. In the following subsections, 5-day averages of 850hPa wind and precipitation were constructed from the model simulations. Beginning in April, prior to the start of precipitation over the Indian subcontinent (Fig. 5), the sequence of pentad averaged 850hPa wind and precipitation fields were examined in tandem for an individual simulation, and those periods (regardless of the time of occurrence) that most resembled the sequence of monsoon landmarks presented in Luo and Yanai (1983) were selected for presentation in Fig. 7. We will first consider the Indian monsoon and return to the East Asian monsoon in Section 5.

b. Preonset phase

Two dynamical factors observed at the 850hPa level seem to be of dominant importance: 1) the Somali jet and the southwesterly flow over the Arabian Sea is the primary factor that gives rise to the orographic precipitation along the west coast of India, and 2) the trough that forms over the Bay of Bengal and the associated cyclonic disturbances give rise to the precipitation over the northeastern portion of the subcontinent.

During the preonset phase of the Indian monsoon the Bay of Bengal trough is located near the Burma/Thailand border, and results in precipitation greater than 10mm day^{-1}. The upwind flank of the trough is dominated by northwesterly winds that run parallel to the Tibetan Plateau, which extend from the Arabian Sea, over subcontinent and into the Bay of Bengal (Luo and Yanai 1983). The T106 simulation simulates these circulation features, Fig. 7a, with flow parallel to the 1500m isoline of the southwestern rim of the Himalayas, and the general tendency for inflow towards the Tibetan Plateau. This latter feature is not as pronounced as in the observations. T42 only satisfies the preonset criteria of simulating northwesterly flow over the Arabian Sea and the subcontinent (Fig. 7b). This flow however, does not extend into the Bay of Bengal. Instead, southwesterly flow is calculated for the Bay of Bengal, as early as mid-April, with the trough located near the east coast of India. Due to the better resolved trough in the T106 simulation, Burma and Thailand receive generous amount of rainfall, consistent with the Luo and Yanai (1983) preonset period, while in T42 the displacement of the trough results in minimal moisture flux convergence, with precipitation rates below 1mm day^{-1} in this region. Because of the westward displacement of the trough in T42, the region of most intense rainfall is situated near the Assam Plain (90-95°E, 20-25°N), a feature that usually occurs during the onset phase. During the T42 preonset period of late April/early May, heavy rains are simulated (Figs. 7b and 5c) over the southern and northeastern sections of India. Early rains are also evident in the T106 simulation during the second week of May, however, they are generally confined to the southern continent and the Arabian Sea where the northwesterlies intersect the flow from the south.

Additional noteworthy features Luo and Yanai (1983) include the presence of persistent northeasterlies in the Tarim Basin (85°E, 40°N) during the preonset stage; these are resolved in the T106 simulation. Perhaps the use of mean orography rather

than the envelope orography used in these simulations may improve these results, particularly in the coarser resolution runs. MONEG recently addressed the use of mean vs. envelope orography, with Shukla and Fennessy (1992) concluding mean orography led to a superior simulation of the monsoon and its' interannual variations.

c. Onset and active phase

The onset and active phases of the monsoon are marked by the development of southwesterly flow along the west coast of India which is initiated by cyclonic activity in the Arabian Sea and a shift of the trough from the Burma region to the east coast of India (Yin 1949). Associated with this is the generation of a cyclonic vortex in the foothills of the Himalayas near Bangladesh (Krishnamurti et al. 1981, Luo and Yanai 1983). In both T106 and T42, Figs. 7c and 7d, an Arabian Sea cyclone initiates the establishment of the prevailing monsoon circulation during the onset phase. These cyclones are associated with rains over southern India that subsequently move north and blanket the west coast of India during the active phase of the monsoon (Figs. 7e and 7f). The T106 simulation is most adept at simulating the Himalayan cyclone as the trough makes landfall at this time (Fig. 7e). The Assam Plain receives realistic precipitation at this time as a result of the generation of southerlies near 90°E, 20°N. Additionally, the central portion of the cyclone is associated with large amounts of precipitation (Luo and Yanai 1983). In T42, the cyclone is displaced 10° to the west over India, and is actually a remnant of a disturbance that developed further to the west, and is inconsistent with the Luo and Yanai (1983) findings. The Assam Plain continues to receive abundant rainfall, as it did incorrectly during the preonset period, with the central portion of the cyclone devoid of precipitation due to the influx of dry air from the northwest. T42 is apparently unable to simulate this synoptic scale sequence in the Himalayan foothills that is an important component of the monsoon over the eastern portion of the subcontinent because of its propensity for early establishment of the Bay of Bengal trough. This bias also occurs during year 2 of the extended T42 simulation and appears to be a systematic shortcoming of this resolution.

d. Break and re-establishment phase

Subsequent to the active monsoon period a break period develops, during which time the precipitation along the trough decreases, and the northern and eastern por-

tions of the country become drier. The trough then begins to re-establish in the Bay of Bengal and migrates northwestward as the monsoon enters another active stage. T106 produces a break period during the latter half of June (Figs. 7g and 5a) while T42 enters a break during the time of normal onset (Das 1984) in late May and early June (Figs. 7h and 5c). The spatial characteristics of the simulated breaks and renewed active phase (Figs. 7i and 7j) are similar in both T106 and T42, but as noted earlier, T106 is superior at simulating the propagation of cyclonic vorticity associated with the trough migration (Fig. 6).

e. Monsoon cessation

A major shortcoming of the Indian monsoon simulation in the T42-T106 simulations is the abrupt cessation of significant precipitation during the latter portion of the monsoon season. Relative to T21, the higher resolutions show an increased sensitivity and greater reliance on the cross-equatorial moisture flux, probably as a result of systematic differences in the low-level flow seen in Fig. 4. In the JJA time mean, T42-T106 do indeed have a larger cross-equatorial vertically integrated moisture flux than T21, while suffering from a 20% reduction in moisture flux over the Arabian Sea relative to T21 (not shown). Hence, in T42-T106 a larger fraction of the precipitable water has its origin in the southern Indian Ocean. The reduced moisture flux over the Arabian Sea is related to several shortcomings of the T42-T106 simulations. Relative to T21 and observations, the low-level air temperature over the Arabian Sea is too cold, and the low-level winds are too weak and displaced to the north. These conditions serve to limit the surface evaporation. The northward displacement of the low-level flow is in turn related to the failure of T42-T106 to simulate a temperature maximum to the east of 70°E near 30°N. Rather, it is located primarily to the north and west of the Arabian Sea, and during the course of the monsoon season the westerly jet migrates towards this local. As the precipitation in the southern tropical Indian Ocean (Fig. 1) increases, the cross-equatorial vertically integrated moisture flux becomes less than that simulated by T21, further reducing the moisture supply into the northern hemisphere, at which time the monsoon essentially ceases. Tao and Chen (1987) have established the importance of the moisture flux from the southern tropical ocean for rainfall over China. However, its role in the Indian monsoon needs to be clarified.

5. Regional Precipitation and Large Scale Flow over the Plains of China

a. Precipitation and 500hPa circulations

In summer, heavy rains occur over the region extending northeastward from the edge of the Tibetan Plateau to the Pacific coast, and they cover the Yangtze River Valley. In a normal year these "Mei-yu" or Plum rains become established in mid-June and last until mid-July. The observed precipitation distributions as reconstructed by Legates and Willmott (1990) are shown in Figs. 8i and 8j, for June and July respectively. In June rains exceeding 5mm day^{-1} cover the southern coast and the Yangtze Valley. During July (Fig. 8j) the band of heavy precipitation is seen to be shifted northward. Figures 8a-h show the ECMWF simulated precipitation for June and July for T21-T106. In T42 (Figs. 8e-f) and T63 (Figs. 8c-d) zones of heavy precipitation over the Yangtze Valley are simulated in June but are seen to be largely absent during July. In T106 (Figs. 8a-b) heavy precipitation in the plains of China is simulated in both months, although the location of the heaviest rains in June is displaced northward in comparison with observations. The results for T21 (Figs. 8g-h) preclude recognition of regional patterns over this area due to the coarseness of its resolution.

The Mei-yu rains are produced along a quasi-stationary front that is formed in a zone of confluence between the monsoon winds from the ocean and northerly flow associated with the polar front (Lau and Li 1984). Figures 9a-j compare geopotential heights and winds at 500hPa for June and July in the T21-T106 simulations and the ECMWF analyses. The ECMWF analyses (Figs. 9i-j) show eastward deflection of the monsoonal wind east of the Tibetan Plateau. The T106 simulation (Figs. 9a-b) produces a more intense trough in this region, clearly portraying the confluence between the southerly and northerly winds. The T63 model (Figs. 9c-d) simulates this confluence in June, but in July the winds are southerly resulting in a lack of sufficient convergence and the deficient precipitation in the Yangtze Valley (Fig. 8d). The June simulation by T42 (Fig. 9e) gives a reasonable depiction of the confluence zone but in July (Fig. 9f) the flow near 110°E has a negligible eastward component south of 30°N which results in dry conditions in the Yangtze Valley and rains to the north (Fig. 8f).

The second year of T42 exhibits similar deficiencies as those seen in Figs. 8e-f and 9e-f, particularly with respect to the flow at 500hPa. This suggests that T42 is unable to properly simulate the large-scale frontal interactions associated with Mei-

yu precipitation. These features will be addressed in more detail in Section 5c, where we examine the dominant modes of Mei-yu precipitation variability through empirical orthogonal function analysis.

b. Influence of the Tibetan Plateau on vertical velocities

The vertical flows across different sections of the Tibetan Plateau are sensitive indicators of the regional scale circulation and the rainfall distribution. Simulation of the direction and strength of the vertical velocity is an important measure of the skill of a model in describing the regional meteorology. Figure 10 gives the simulated June monthly mean East-West vertical cross-section of vertical velocity near 32°N. The observations (Fig. 12a of Luo and Yanai 1983) indicate rising motion over the Plateau, centered near 93°E, between 300-400hPa, with maximum upward velocity of 0.13 Pa s^{-1}. To the east, an orographic maximum is located along the eastern slope of the Plateau near 105°E-115°E, and further east between 115°E-125°E, corresponding to the Mei-yu frontal zone. Above 700hPa, rising motion in T106 (Fig. 10a) simulates this structure, however, the orographic uplift is stronger than observed, while that associated with the heating over the Plateau is weaker. T63 simulates similar upward velocities over the Plateau and the China Plain but the two regions are separated by a zone of descending motion. T42 and T21 (Figs. 10 c-d) only simulate the orographic uplift. Near the western border of the Plateau, only T106 simulates the subsidence that penetrates to the surface over northwest India. The upward motion over the Indus Valley (70°E-75°E) is simulated in all of the models.

The zonal profile of vertical velocity near 92°E is given in Fig. 11. In the observations (Fig. 12b of Luo and Yanai 1983), intense ascending motions occur over the Tibetan Plateau and over the Assam Plain near 25°N. To the north of the Plateau, near 40°N-45°N, pronounced descending motion is readily apparent. All of the simulations represent the upward motion associated with the Assam Plain. This results primarily from the onshore flow from the trough in the Bay of Bengal where low-level confluence first encounters topography. The model systematically overestimates the extent of the uplift, producing a much broader region of ascent not indicated in the FGGE data. The model underestimates the uplift associated with the local heating over the center of Tibetan Plateau. Only T106, Fig. 11a, hints at a locally distinct re-

gion of uplift to the north of 30°N seen in the observations. In the coarser resolution simulations, the upward motion is associated with the orographic influence of the Assam Plain. Near the northern edge of the Plateau, the models generally simulate descent. However, T21-T63 place the core of the maximum subsidence northward of 45°N, while in T106 and the FGGE data, the major subsidence is located near 42°N.

In this comparison, the high resolution of T106 offers a clear advantage in reproducing important regional features of vertical motion that are found in the FGGE observations. All of the major features of the observations are simulated by T106 while the lower resolution versions produce significant distortions of several branches of the vertical motion.

c. Seasonal Cycle and Mei-yu modes in East Asian precipitation

Empirical orthogonal function (EOF) analysis may be used to identify dominant patterns of precipitation over China and how they change with time. Lau et al. (1988) performed such an analysis on a 10-year climatology (1961-70) of 10-day averaged Chinese station precipitation for the period April-September. Their analysis identified the seasonal cycle, as well as a hierarchy of modes that characterize the evolution of the Mei-yu. A similar analysis of 10-day averaged precipitation for the period April-September from the resolution simulations is shown in Fig. 12. The first EOF's from the simulations correspond to the "broad-scale seasonal mode," the first EOF in Lau et al. (1988). In T106 and T42, this mode consists of a north-south dipole centered near 30°N, as in observations, which explain approximately 30 percent of the total variance. The principal component (PC) time series of the first EOF indicates that the simulated seasonal cycle evolves in a similar manner as observed. Positive precipitation departures (with respect to the April-September mean) occur over the southern portion of China during the early portion of the record. During the later portion of the period the rain shifts to the north and then tends to diminish. T63 and T21 (Figs. 12b and 12d) are exceptions, failing to demonstrably resolve the spatial dipole. Rather, the seasonal cycle mode consists of a precipitation monopole that waxes and wanes with time. The first EOF and PC of the second year of the T42 simulation exhibit similar features to those presented for the first year (Fig. 12c). Thus, with regard to the seasonal mode, the interannual variability is less than the differences among the models suggesting that T63 and T21 are true outliers with regard to the simulation

of the seasonal cycle. These findings indicate that T42 and T106 best exhibit the seasonal mode of precipitation over China during the East Asian monsoon.

Examination of additional EOF's indicate that the dominant "Mei-yu" mode found by Lau et al. (1988) is represented by EOF 3 in the simulations (Fig. 13). They describe it as "a somewhat zonally oriented structure with alternating highs and lows stretching from the extreme northern and southern extent of China." In the observations, the associated temporal variability is essentially bimodal, whereas in the model (particularly T106) higher frequency variations are evident. The observed bimodal PC is due to the averaging of 10 years of 10-day mean data by Lau et al. (1988). In this case slight differences in the phasing of the oscillating rainband from vear to year are averaged out, resulting in a redder spectrum than that for an individual year. In T106, Fig. 13a, we see that the Mei-yu mode consists of an oscillation of the rainband that gives rise to periods of enhanced rainfall over the Yangzi River Valley. While the pattern in T63 also shows alternating signs, Fig. 13b, the phasing of precipitation is essentially reversed relative to the observations as indicated by the PC. This is confirmed by the July mean precipitation given in Fig. 8d. This deficit arises due to the westward extension of the subtropical high over eastern China as seen in the 500hPa geopotential height given in Fig. 9d. T106, Figs. 9a-b, exhibits the best agreement with observations (Fig. 9i-j) in this respect in that the subtropical high, here denoted by the 5840 geopotential meter (gpm) isoline, shifts northward in July relative to June as observed (5880 gpm isoline). In T42, not only does this high make landfall, but the positive node of the Mei-yu mode, Fig. 13c, is displaced to the west resulting in little precipitation in Yangtze River Valley (Fig. 8f). The coarse resolution of T21 precludes simulation of a spatial eigenvector distribution that can be identified as the Mei-yu mode.

The time evolution of precipitation over the Yangtze River Valley (110°E-125°E, 25°N-32.5°N) can be more clearly seen in Fig. 14, which gives average daily precipitation in this region. Quasi-periodic variations of rainfall over this region, especially pronounced in the T106 simulation, result from north/south oscillations of the rainband seen in Fig. 13a. These oscillations are superimposed over a background deposition rate of approximately 4mm day^{-1}, similar to that observed by Luo and Yanai (1983). At the lower resolutions, the difference in the temporal variability noted in the EOF/PC patterns becomes more evident, as does the tendency for precipitation to be

excessive from March to May. Early precipitation over the Yangzi River Valley is also evident in the second year of the T42 simulation (not shown).

The dynamics that give rise to the pre-Mei-yu rainfall is also different among the resolutions. In T42, as seen in Fig. 7, the trough over India establishes too early. The flow arising from this trough extends into China, giving rise to the preseason rainfall in the Yangtze River Valley. By contrast in T106, precipitation occurring prior to mid-May is associated with rainbands that propagate southeastward from Mongolia and Siberia, and are related to the last vestiges of the winter monsoon circulation. Thus, the persistent and early nature of T42 to generate the Bay of Bengal trough results in downstream effects causing China precipitation to be inherently different in T42 relative to T106 and the observations during the preseason.

The three resolutions of the ECMWF model discussed here simulate important features of the Mei-yu precipitation and its associated circulation. In this comparison we see that the highest resolution model, T106, offers a clear improvement in simulating the spatial and temporal distribution of rainfall during the East Asian monsoon.

6. Discussion

The goal of this paper has been to investigate the horizontal resolution dependence of the high frequency synoptic scale variations that are associated with the Indian and East Asian summer monsoon. Given that these phenomena generally evolve through a characteristic sequence of events, it is important that a model be able to simulate these important features of monsoon development for validation purposes. Examination of synoptic scale variations has proven to be a sensitive indicator of model performance for the purpose of validation. It has enabled us to highlight fundamental differences in the manner in which one model generates its mean state when run through a scenario that consists of several different horizontal resolutions. On time scales of a month or longer the most demonstrable differences occur between T21 and T42, the latter of which has been judged adequate for climate studies (Tibaldi et al. 1990, Boyle 1993, Gleckler and Taylor 1993, and Phillips et al. 1994). However, in order to evaluate higher frequency variations, our evidence indicates that T106 is the superior model. In this study, the climate of T42 arises from synoptic scale variations that are different in character from the observations and T106. This suggests

that T42 is inadequate for studies of the summer monsoon. In particular, Figs. 6, 7, 13, and 14 demonstrate that T42 is incapable of simulating the high frequency characteristics of the Indian and Mei-yu monsoons. While the recommendation of employing T106 might be considered overly excessive, it must be tempered by the limitations of the study. The study sample size of one model, run through 1 or 2 annual cycles at four horizontal resolutions is a less than robust construct from which to draw such a generalized (and computationally expensive) conclusion. We hope however, that this study will bring to light the importance of evaluating high frequency time scales as an important component of the climate system.

This is but one step in evaluating how well GCMs simulate the tropical transience. Previous work has demonstrated the viability with which the T106 version of this model simulates tropical easterly waves and low frequency variability when integrated in perpetual mode (Slingo et al. 1992). Future work will be aimed at evaluating such behavior in the seasonal cycle integrations presented in this paper and later in the multitude of AMIP simulations.

Acknowledgments

We gratefully acknowledge the ECMWF for making their forecast model available for this research and for reviewing this manuscript. We wish to thank Drs. Ming-Hua Zhang and Benjamin Santer for helpful discussions. The simulations were performed at the National Energy Research Supercomputer Center. This work was supported by the Environmental Sciences Division, Office of Energy Research, U. S. Department of Energy and performed by the Lawrence Livermore National Laboratory under U.S. Department of Energy Contract W-7405-Eng-48 with the University of California and contract DEFG0285ER60314A007 with the State University of New York at Stony Brook.

References

Alexander, R. C., and R. L. Mobley, 1976: Monthly averaged sea surface temperatures and ice-pack limits on a 1-degree global grid. *Mon. Wea. Rev.*, **104**, 143-148.

Blondin, C., and H. Böttger, 1987: The surface and sub-surface parameterization in the ECMWF forecasting system: Revision and operational assessment of weather elements. ECMWF Tech. Memo. No. 135, European Centre for Medium-Range Weather Forecasts, Reading, England.

Boer, G. J., and M. Lazare, 1988: Some results concerning the effect of horizontal resolution and gravity-wave drag on simulated climate. *J. Clim.*, **1**, 789-806.

Boville, B. A., 1991: Sensitivity of simulated climate to model resolution. *J. Clim.*, **4**, 469-485.

Boyle, J. S., 1992: Sensitivity of dynamical quantities to horizontal resolution for a climate simulation using the ECMWF (cycle 33) model. *J. Clim.*, **6**, 796-815.

Das, P. K., 1984: The monsoons-a perspective. Golden Jubilee Publications, Indian National Science Academy.

Gadgil, S., and J. Srinivasan, 1990: Low frequency variation and tropical convergence zones. *Meteorol. Atmos. Phys.*, **44**, 119-132.

Gates, W. L., 1992: The atmospheric model intercomparison project. *Bull. Amer. Meteor. Soc.*, **73**, 1962-1970.

Gleckler, P. J., and K. E. Taylor, 1993: The effect of horizontal resolution on ocean surface heat fluxes in the ECMWF model. UCRL-ID-108553, PCMDI Report No. 3, *Clim. Dyn.* (in press).

Hansen, J., G. Russel, D. Rind, P. Stone, A. Lacis, S. Lebedeff, R. Ruedy, and L. Travis, 1983: Efficient three-dimensional global models for climate studies: Models I and II. *Mon. Wea. Rev.*, **111**, 609-662.

Kiehl, J. T., and D. L. Williamson, 1991: Dependence of cloud amount on horizontal resolution in the National Center for Atmospheric Research Community Climate Model. *J. Geophys. Res.*, **96D**, 10,955-10,980.

Lau, K-M., and M. T. Li, 1984: The monsoon of East Asia and its global associations-a survey. *Bull. Amer. Meteor. Soc.*, **65**, 114-125.

Legates, D. S., and C. J. Willmott, 1990: Mean seasonal and spatial variability in gauge-corrected, global precipitation, *Internat. J. Climatol.*, **10**, 111-127.

Luo, H., and M. Yanai, 1983: The large-scale circulation and heat sources over the Tibetan Plateau and surrounding areas during the early summer of 1979. Part I: Precipitation and kinematic analyses. *Mon. Wea. Rev.*, **111**, 922-944.

Miller, M. J., A. C. M. Beljaars, and T. N. Palmer, 1992: The sensitivity of the ECMWF model to the parameterization of evaporation from the tropical oceans. *J. Clim.*, **5**, 418-434.

Mohanty, U. C., A. Hollingsworth, and S. K. Dash, 1985: Asian summer monsoon circulation statistics: 1979-1984. European Centre form Medium-Range Weather Forecasts, Reading, England.

Morcrette, J.-J., 1990: Impact of changes to the radiation transfer parameterizations plus cloud optical properties in the ECMWF model. *Mon. Wea. Rev.*, **118**, 847-873.

Morcrette, J.-J., 1991: Radiation and cloud radiative properties in the ECMWF operational weather forecast model. *J. Geophys. Res.*, **96D**, 9121-9132.

Newell, R. E., J. W. Kidson, D. G. Vincent, and G. J. Boer, 1972: The general circulation of the tropical atmosphere. Vol. 1, MIT Press, Cambridge, Massachusetts.

Palmer, T. N., G. J. Shutts, and R. Swinbank, 1986: Alleviation of a systematic westerly bias in general circulation and numerical prediction model through an orographic gravity wave drag parameterization. *Quart. J. Roy. Met. Soc.*, **112**, 1001-1039.

Palmer, T. N., C. Brankovic, P. Viterbo, and M. J. Miller, 1992: Modeling interannual variations of summer monsoons. *J. Clim.*, **5**, 399-417.

Phillips, T. J., L. C. Corsetti, and S. L. Grotch, 1994: The impact of horizontal resolution on moist processes in the ECMWF model. UCRL-ID-112719, PCMDI Report No. 8, *Clim. Dyn.* (in press).

Potter, G. L., S. Hameed, J. S. Boyle, and K. R. Sperber, 1993: Effect of spatial resolution on the simulation of regional precipitation in China in a global climate model. UCRL-JC-111835, Proceedings of the AMS Fourth Symposium on Global Change Studies, Anaheim, CA, January 17-22, 1993, 34-37.

Rind, D., 1988: Dependence of warm and cold climate depiction on climate model resolution. *J. Clim.*, **1**, 965-997.

Shukla, J., and M. J. Fennessy, 1992: Some idealized numerical experiments to diagnose the simulated Asian summer monsoon circulation and rainfall. in Simula-

tion of interannual and intraseasonal monsoon variability. WCRP-68, WMO/TD-No. 470., Geneva, Switzerland.

Simmons, A. J., D. M. Burridge, M. Jarraud, C. Girard and W. Wergen, 1988: The ECMWF medium-range prediction models, development of the numerical formulations and the impact of increased resolution. *Meteor. Atmos. Phys.*, **40**, 28-60.

Slingo, J. M., M. Blackburn, J. Thuburn, L. Steenman-Clark, R. Brugge, and B. Hoskins, 1992a: Synoptic validation of climate models: Aspects of variability in the tropics of the UGAMP general circulation model. Proceedings of the ECMWF Seminars on Model Validation. September 7-11, 1992, 265-279.

Slingo, J. M., K. R. Sperber, J.-J. Morcrette, and G. L. Potter, 1992b: Analysis of the temporal behavior of convection in the tropics of the European Centre for Medium-Range Weather Forecasts Model. *J. Geophys. Res.*, **97D**, 18,119-18,135.

Slingo, J. M., M. Blackburn, A. Betts, R. Brugge, B. Hoskins. M. Miller. L. Steenman-Clark, and J. Thuburn, 1993: Mean climate and transience in the tropics of the UGAMP GCM: sensitivity to convective parameterization. *Quart. J. Roy. Meteorol. Soc.* (submitted).

Tao, S., and L. Chen, 1987: A review of recent research on the East Asian summer monsoon in China. Monsoon Meteorology, eds. C.-P. Chang and T. N. Krishnamurti, Oxford Monographs on Geology and Geophysics No. 7, Oxford University Press, New York. Chap. 3, 60-92.

Tibaldi, S., T. N. Palmer, C. Brankovic, and U. Cubasch, 1990: Extended-range predictions with ECMWF models: Influence of horizontal resolution on systematic error and forecast skill. *Quart. J. Roy. Meteor. Soc.*, **116**, 835-866.

Tiedtke, M., 1989: A comprehensive mass-flux scheme for cumulus parameterization in large-scale models. *Mon. Wea. Rev.*, **117**, 1779-1800.

Tiedtke, M., W. A. Heckley and J. M. Slingo, 1988: Tropical forecasting at ECMWF: The influence of physical parametrization on the mean structure of forecasts and analyses. *Q. J. R. Meteor. Soc.*, **114**, 639-664

WCRP, 1992: Simulation of interannual and intraseasonal monsoon variability. WCRP-68, WMO/TD-No. 470., Geneva, Switzerland.

WCRP, 1993: Simulation and prediction of monsoons, recent results. WCRP-80, WMO/TD-No. 546., Geneva, Switzerland.

Yin, M. T., 1949: A synoptic-aerologic study of the onset of the summer monsoon over India and Burma, *J. Meteorol.*, **6**, 393-400.

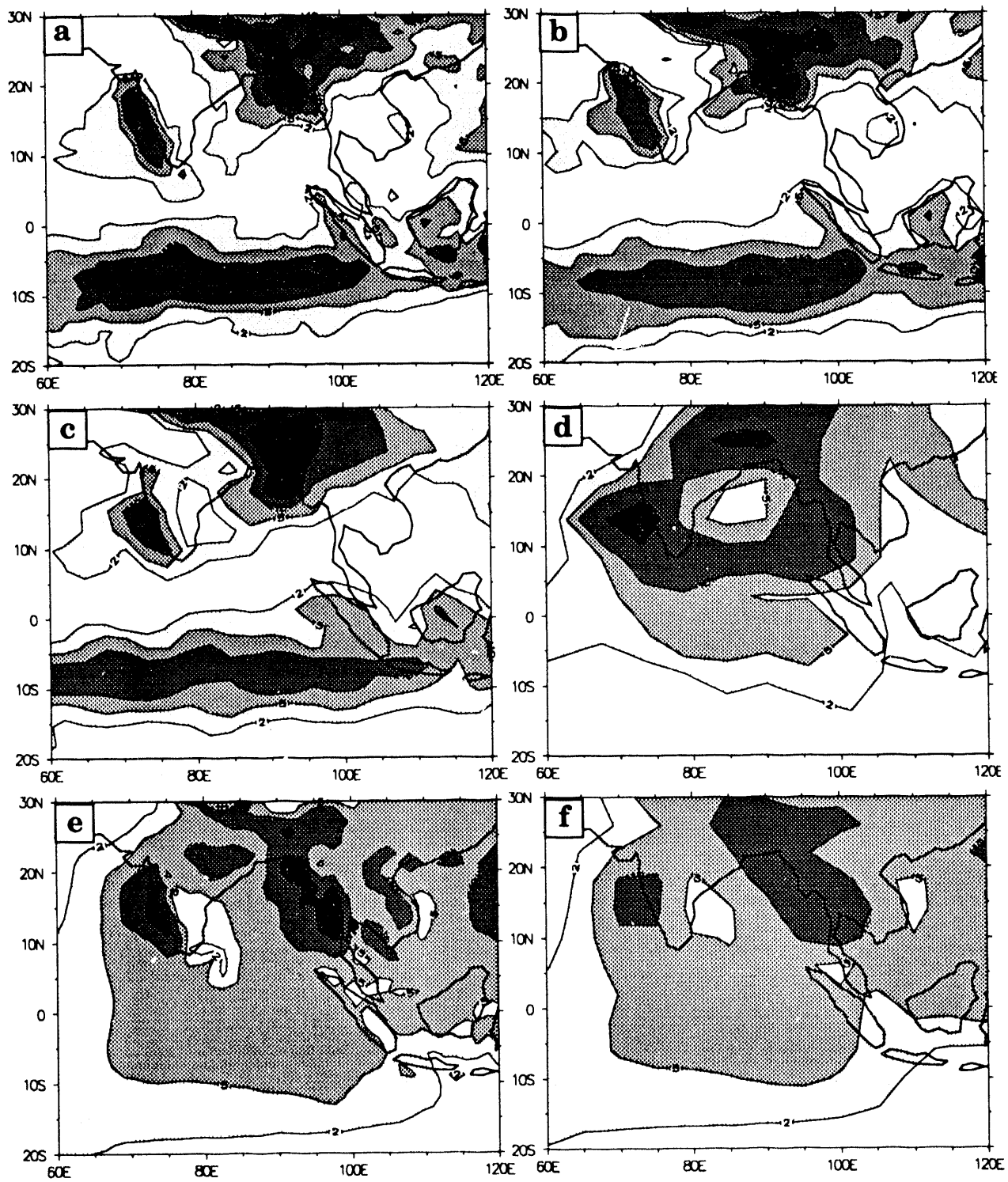

Figure 1. June/July/August mean precipitation rate a) T106, b) T63, c) T42, d) T21, e) Legates and Willmott (1988) and f) Jaeger (1976). Shading denotes precipitation rates in three intervals, 2-5mm day^{-1}, 5-10mm day^{-1}, and $\geq$10mm day^{-1}.

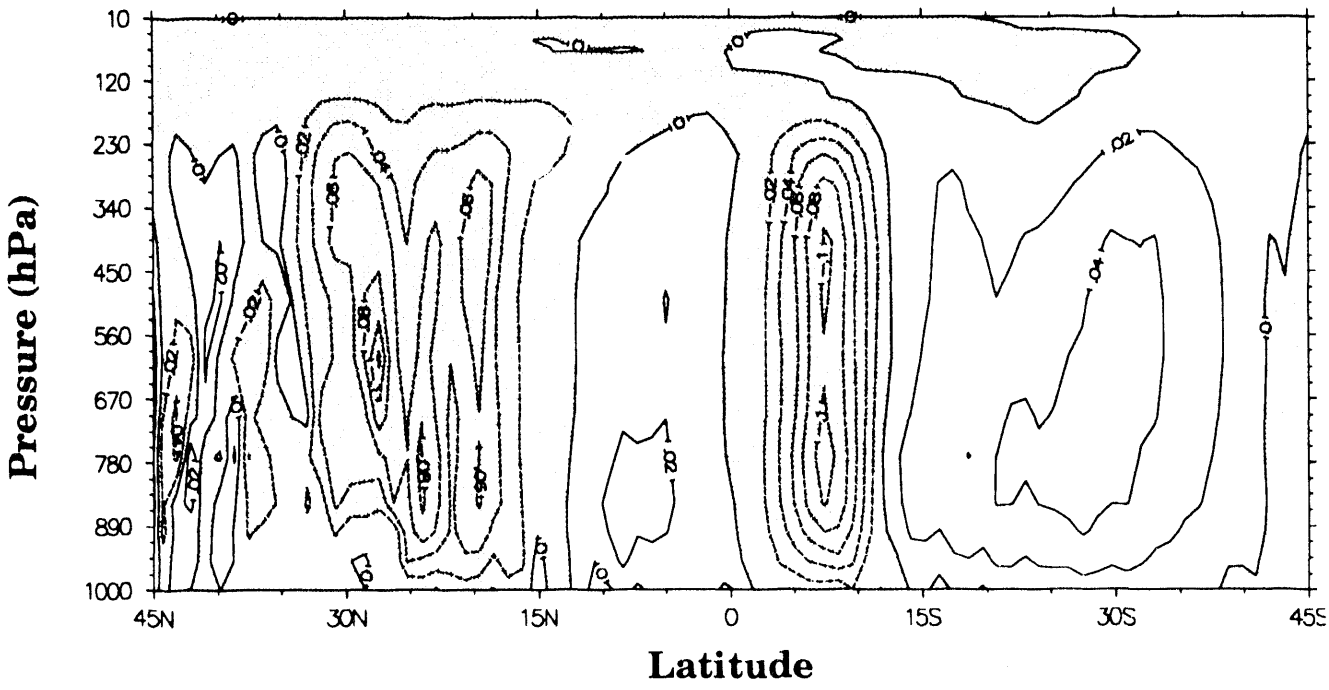

Figure 2. June/July/August mean T106 simulated latitude-height cross-section of vertical velocity averaged between 60°E-115°E. The contour interval is 0.02 Pa s^{-1}. Shading denotes ascent.

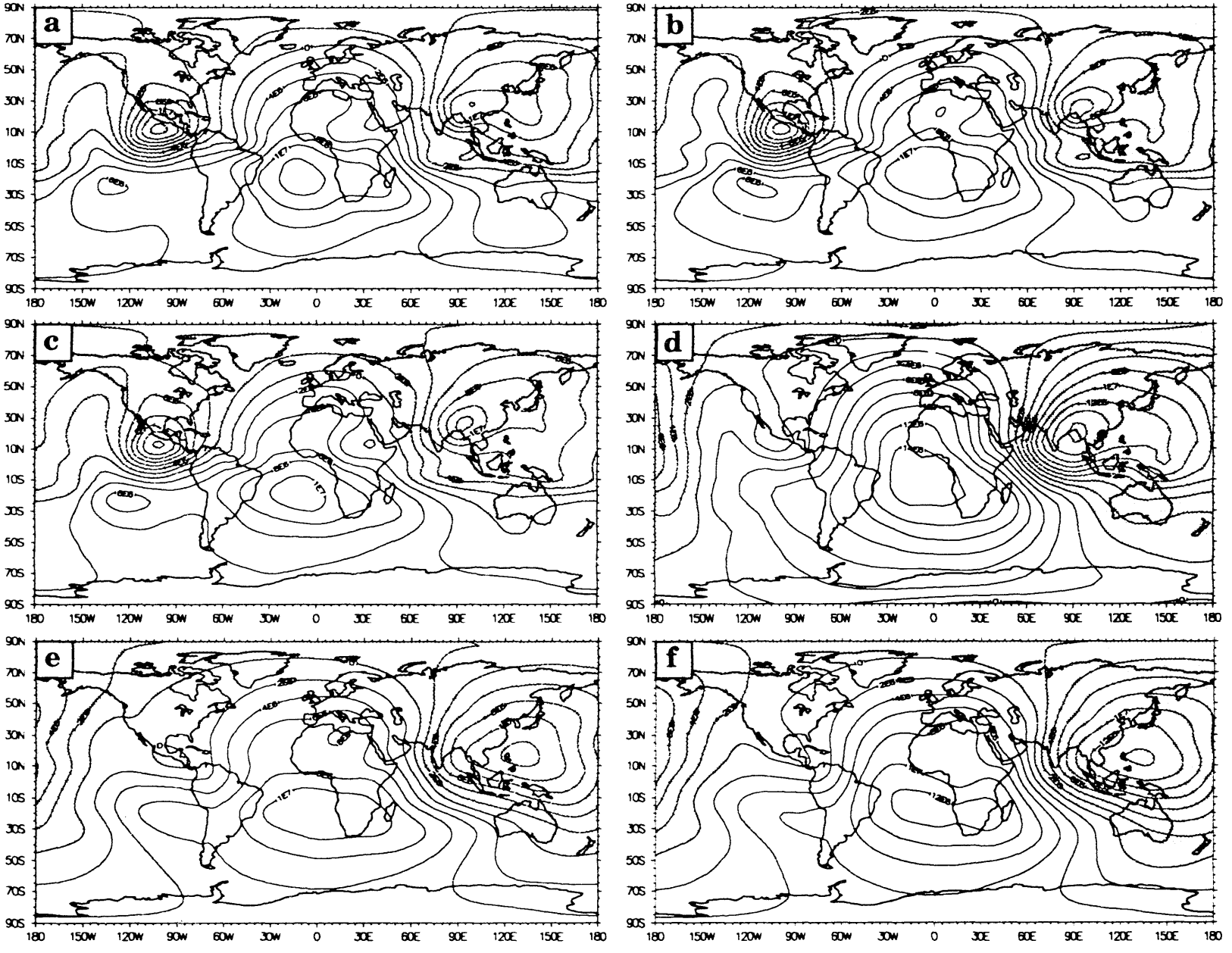

Figure 3. June/July/August mean 200hPa velocity potential a) T106, b) T63, c) T42, and d) T21, e) ECMWF initializations (1980-89), and f) NMC CDDB analyses (1979-88). Negative (shaded) values indicate upper level divergence and the contour interval is 2×10^6 $m^2\ s^{-1}$.

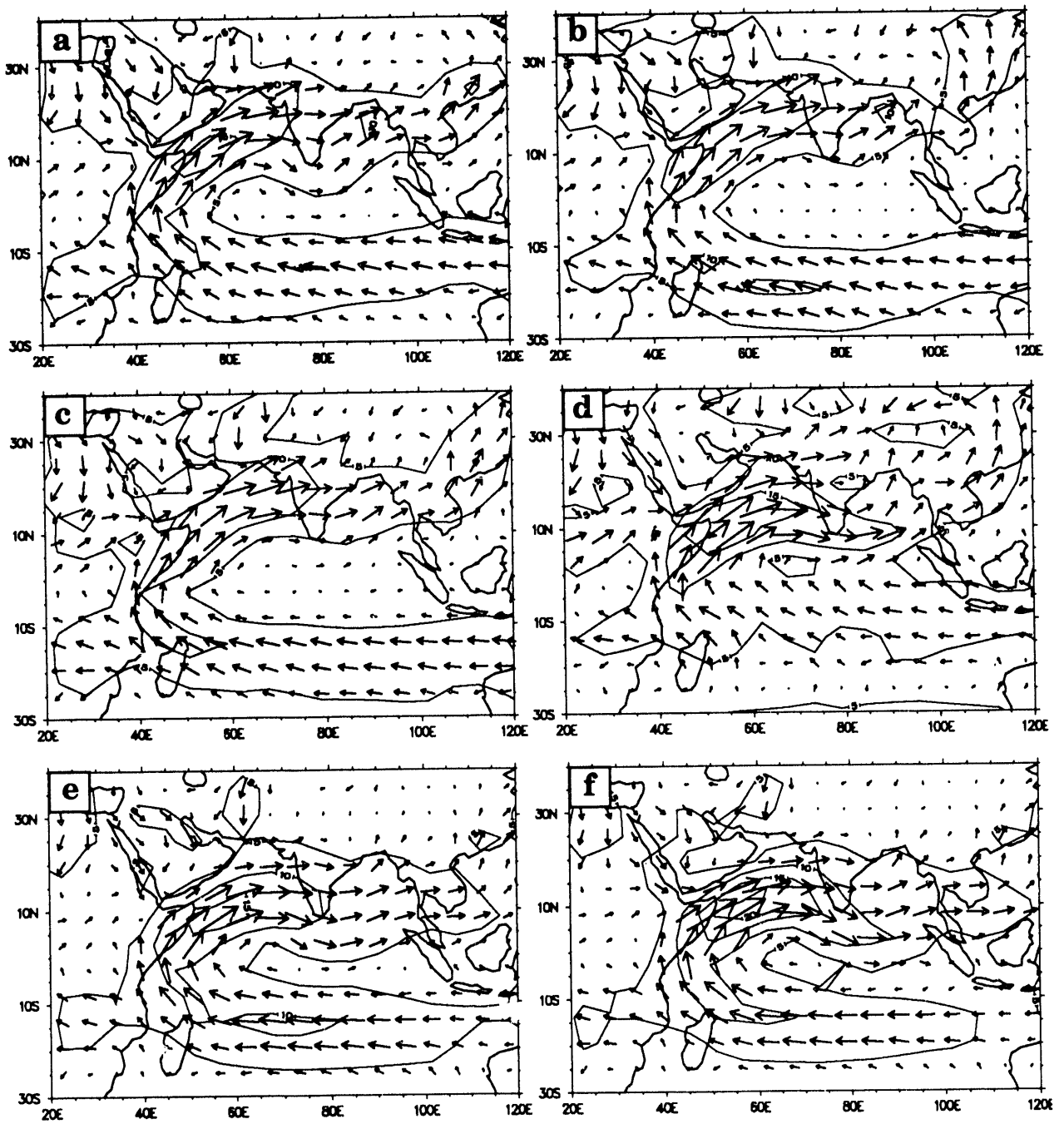

Figure 4. July mean 850 hPa winds (all interpolated to T21 grid) and windspeed a) T106, b) T63, c) T42, d) T21, e) ECMWF initializations (1980-89), and f) NMC CDDB analyses (1979-88). The windspeed is contoured at intervals of 5 m s^{-1}.

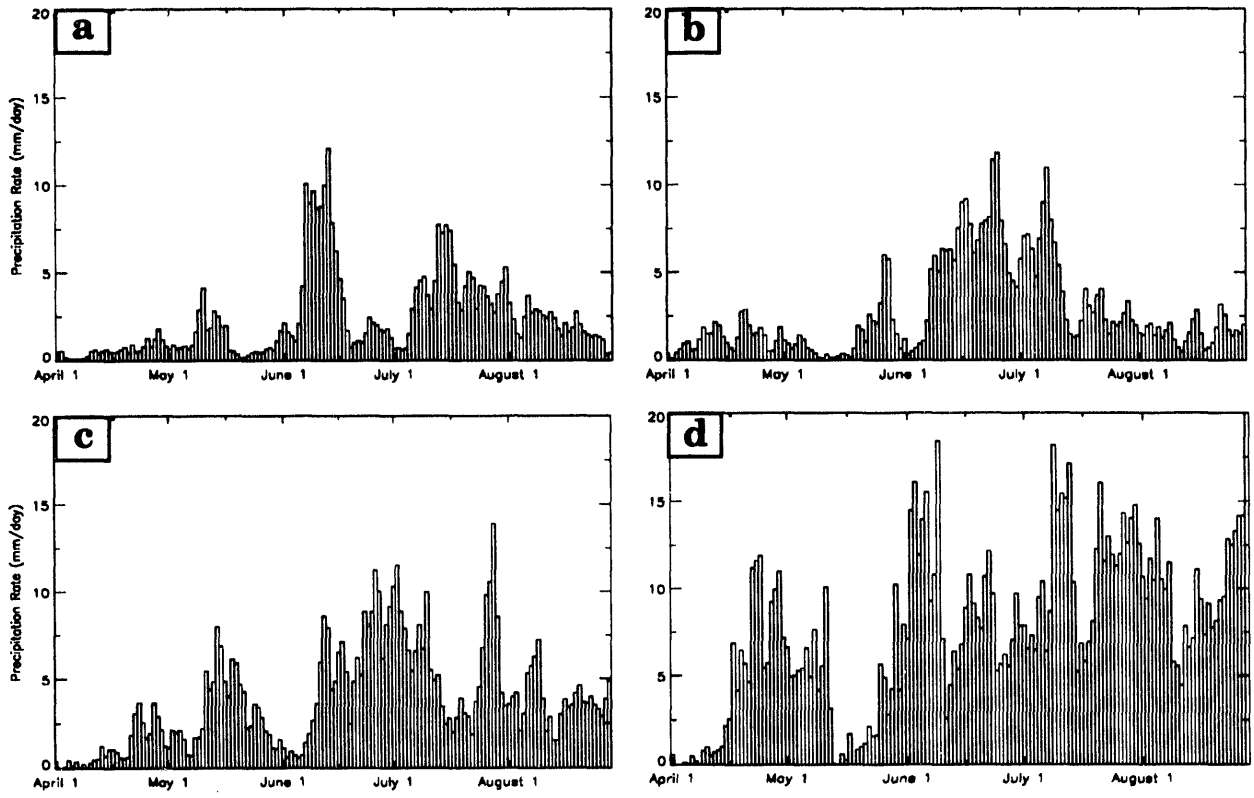

Figure 5. Indian monsoon precipitation index is the area-weighted average precipitation rate (mm day^{-1}) over the Indian subcontinent south of 25°N. a) T106, b) T63, c) T42, and d) T21.

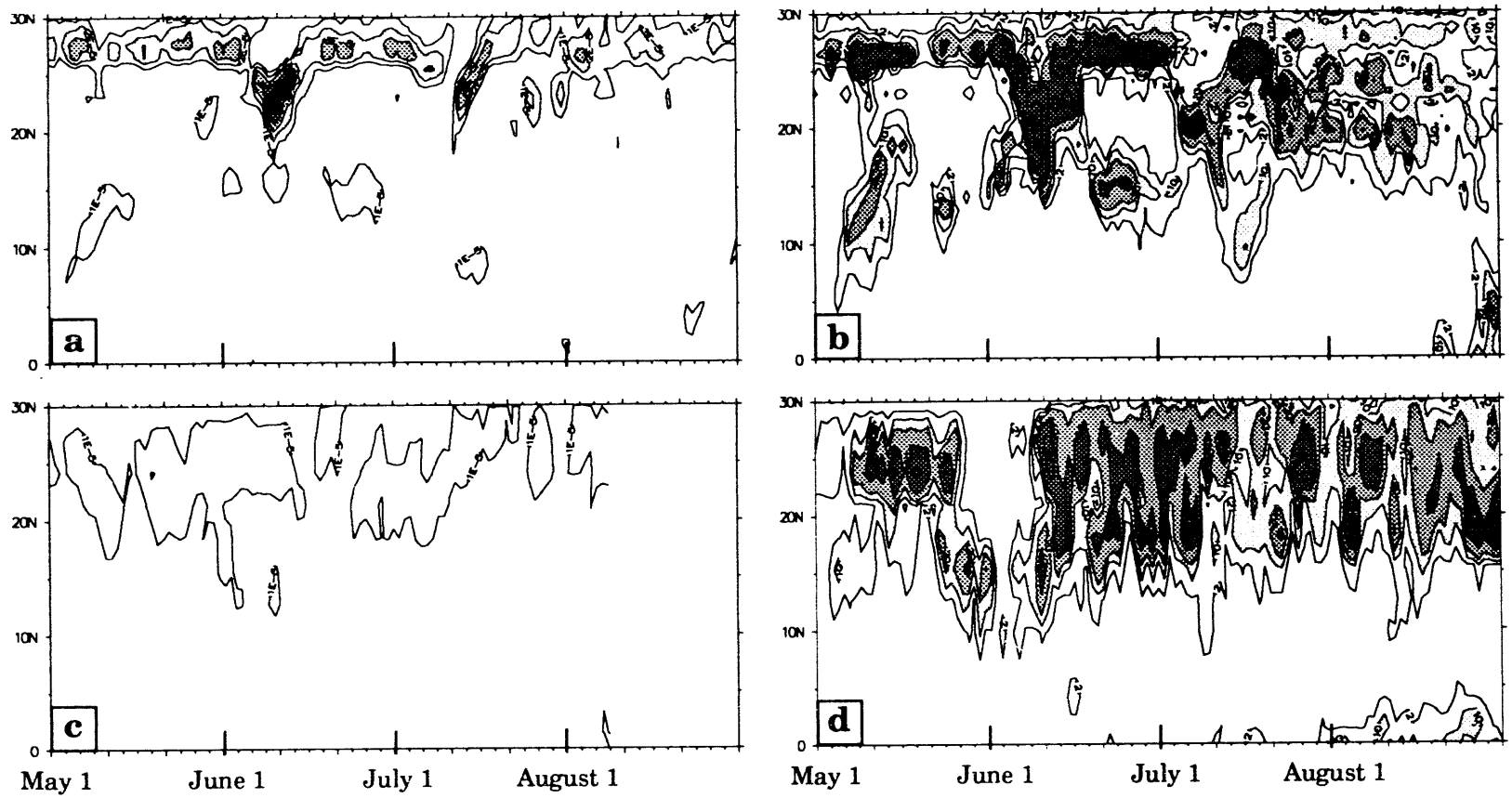

Figure 6. a) Time-latitude diagram of 850hPa relative vorticity averaged between 79-90°E for T106. Contours in excess of 1 x 10^{5} s^{-1} are shaded and shown at intervals of 1 x 10^{-5} s^{-1}, b) time-latitude diagram o f precipitation rate at 90°E. Shading denotes precipitation rates in four intervals, 2-10mm day^{-1} , 10-20mm day^{-1}, 20-40mm day^{-1}, and ≥40mm day^{-1}, c) as (a) for T42, d) as (b) for T42.

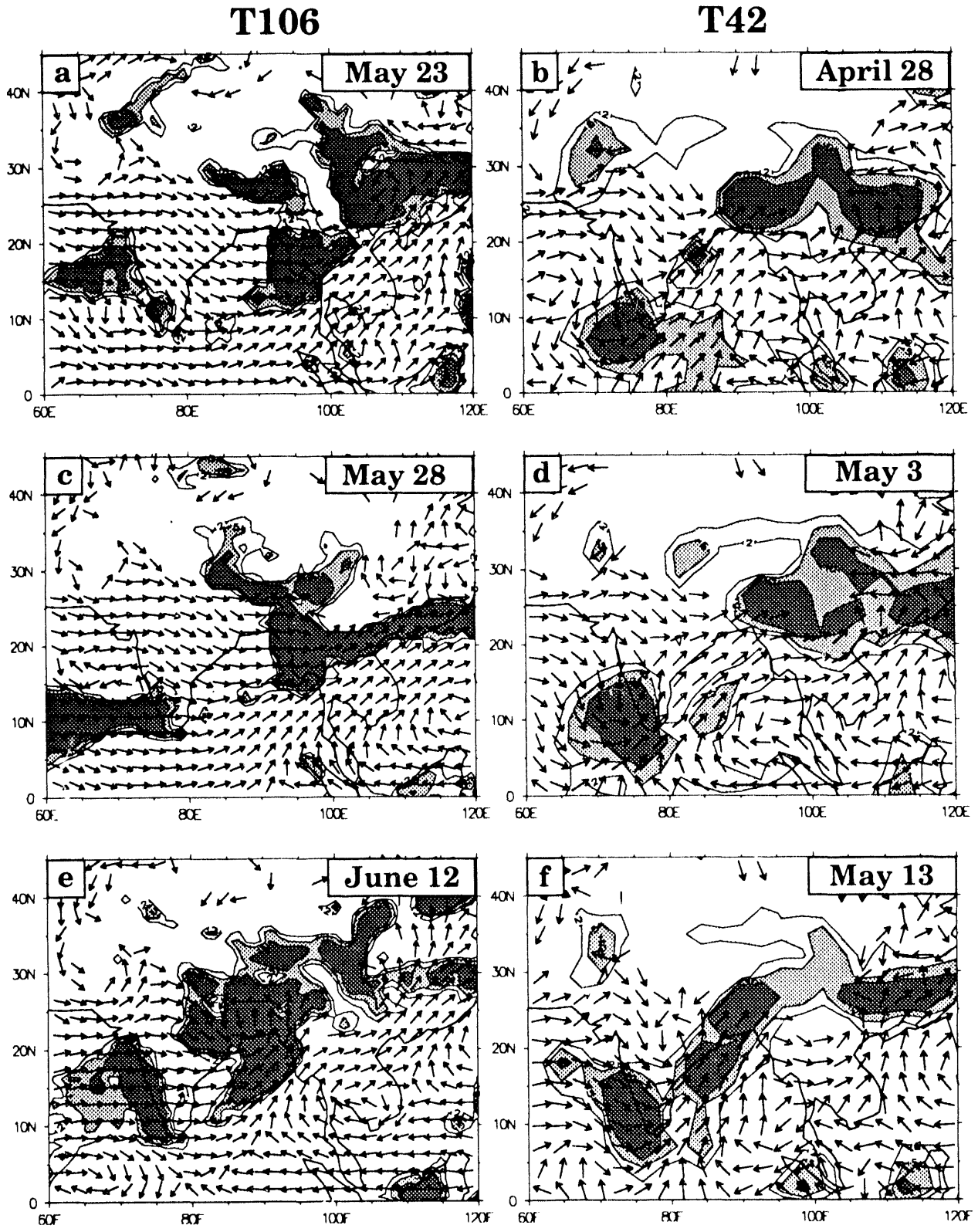

Figure 7. Simulated milestones in the evolution of the Indian monsoon (5-day means). Preonset:

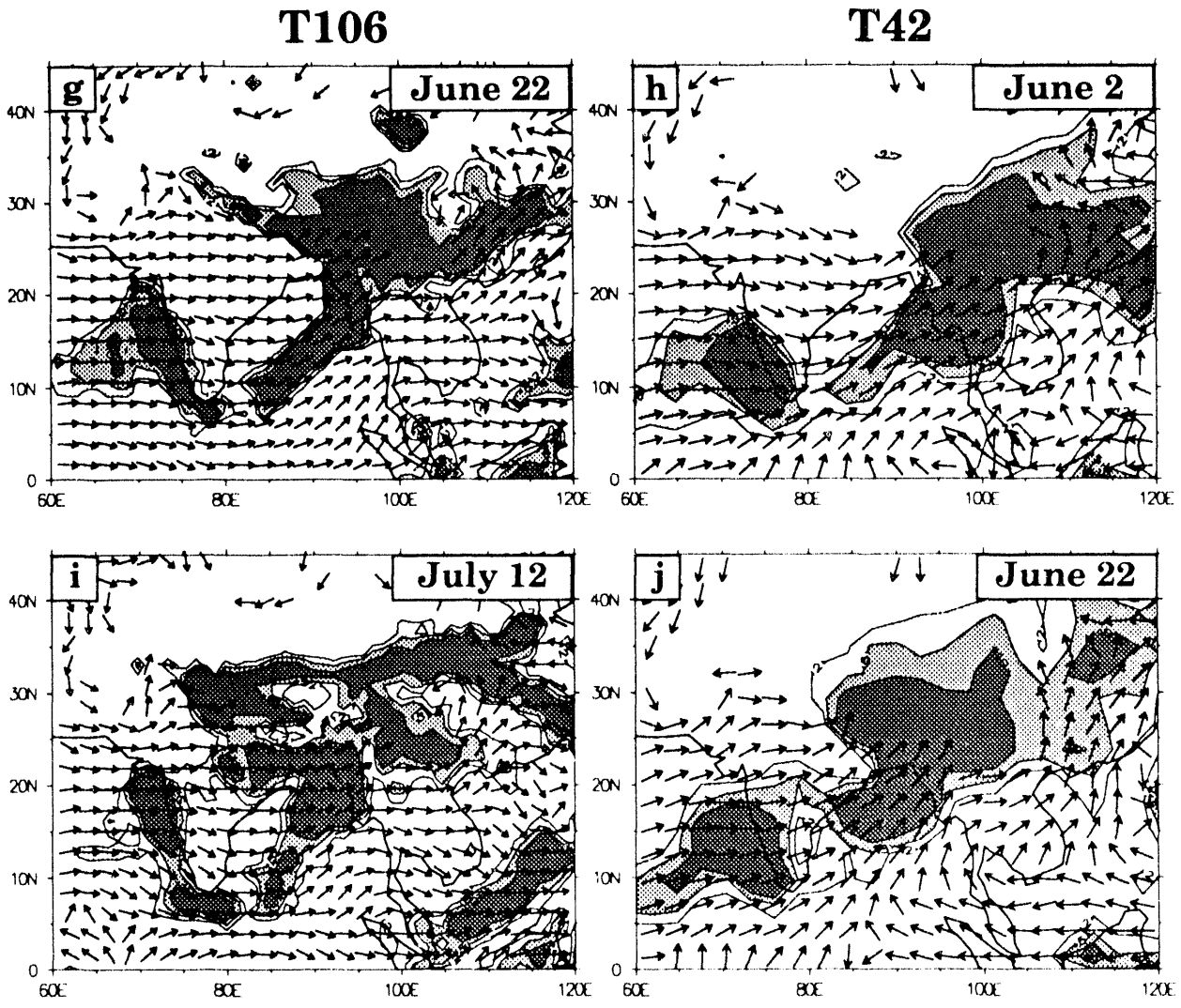

Figure 7 (con't) a) T106, b) T42; onset: c) T106, d) T42; active: e) T106, f) T42; break: g) T106, h) T42; active: i) T106, j) T42. The 850hPa flow is superimposed upon precipitation rate. The wind vectors have been normalized to unit length and every other vector has been plotted for T106 to more clearly show the prevailing flow. Shading denotes rainfall rates in three intervals, 2-5mm day^{-1}, 5-10mm day^{-1}, and $\geq$10mm day^{-1}. Orography in excess of 1500m masks isotachs that are below ground. The given date is the midpoint of the 5-day mean.

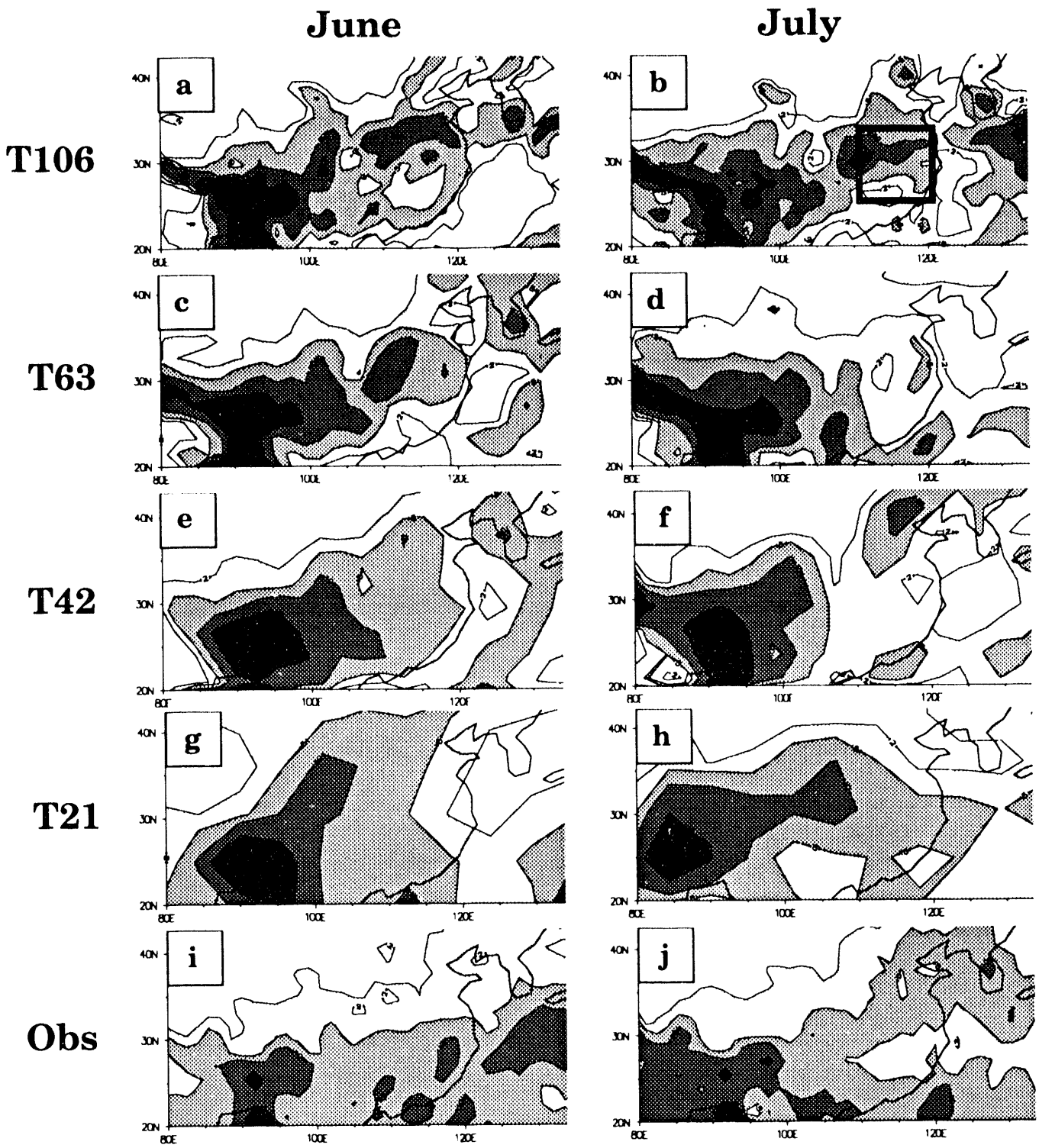

Figure 8. Precipitation distribution (mm day^{-1}), T106: a) June, b) July; T63: c) June, d) July; T42: e) June, f) July; T21: g) June, h) July, observed (Legates and Willmott, 1990): i) June, j) July. Shading denotes precipitation rates in three intervals, 2-5mm day^{-1}, 5-10mm day^{-1}, and $\geq$10mm day^{-1}.

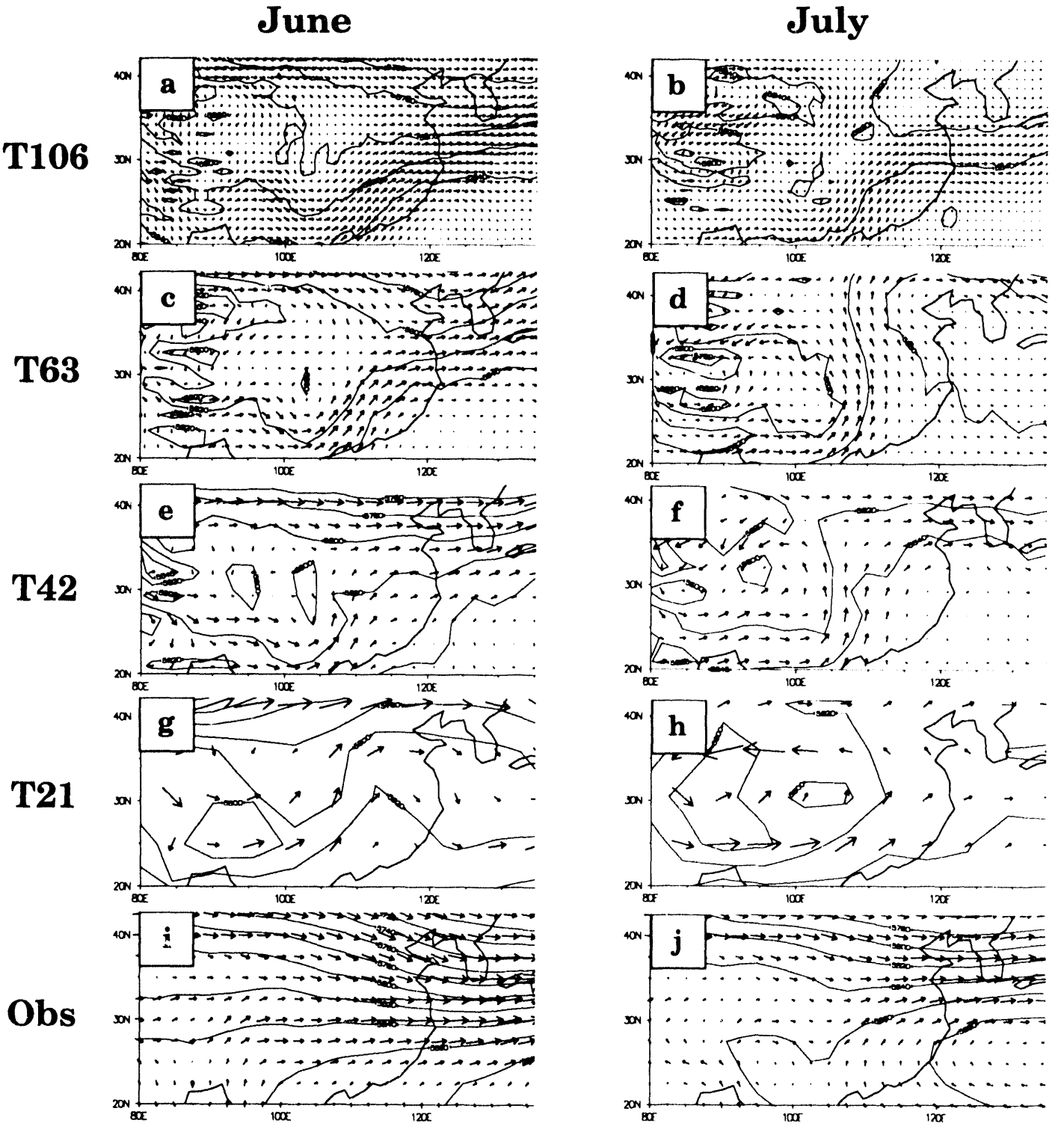

Figure 9. 500hPa winds and geopotential heights (m), T106: a) June, b) July; T63: c) June, d) July; T42: e) June, f) July; T21: g) June, h) July; ECMWF analyses: i) June j) July. The geopotential height is contoured at an interval of 20m.

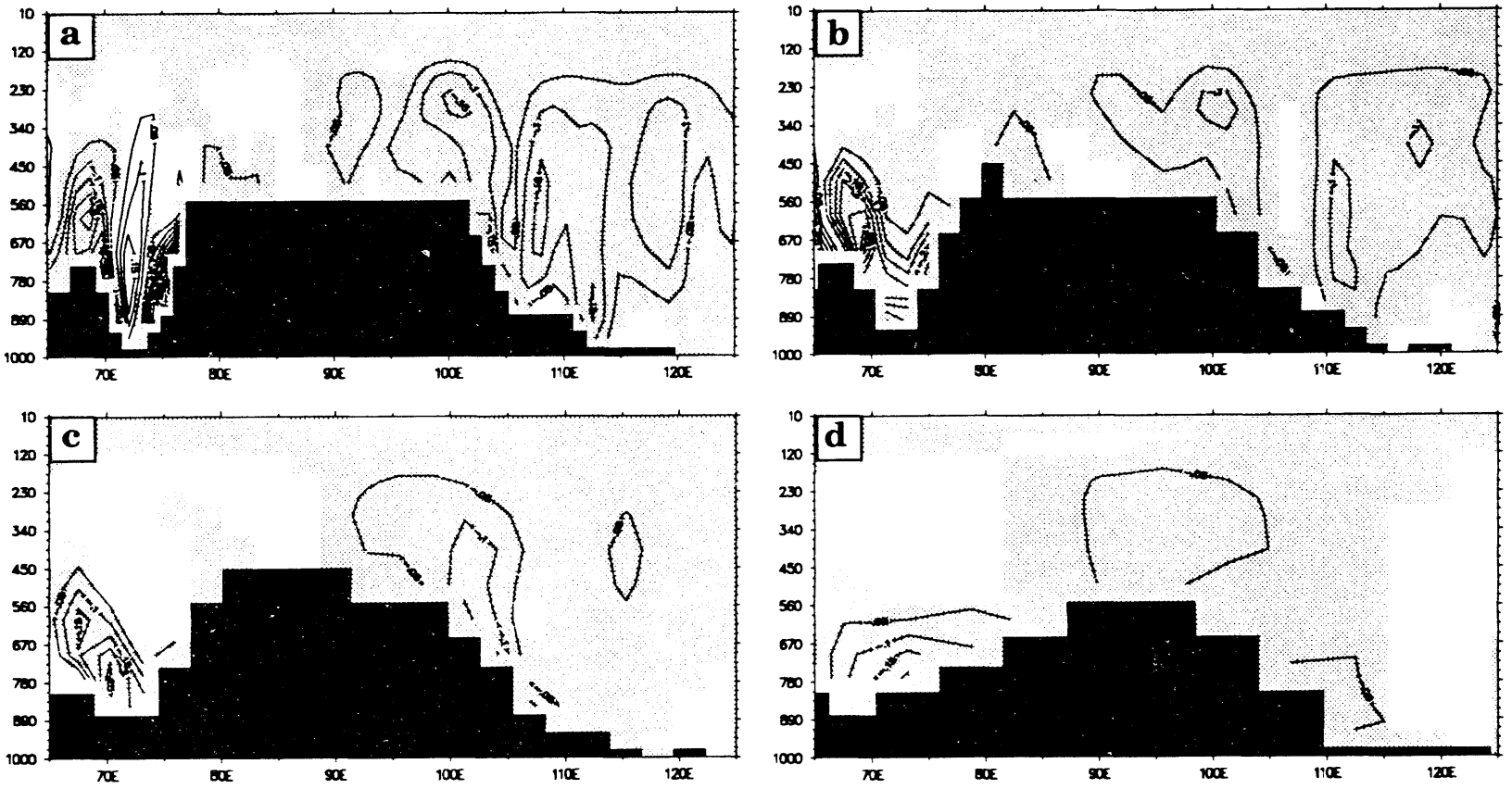

Figure 10. June cross-section of vertical velocity (Pa s^{-1}) near 32°N a) T106, b) T63, c) T42, and d) T21. Light shading denotes ascent and black corresponds to topography.

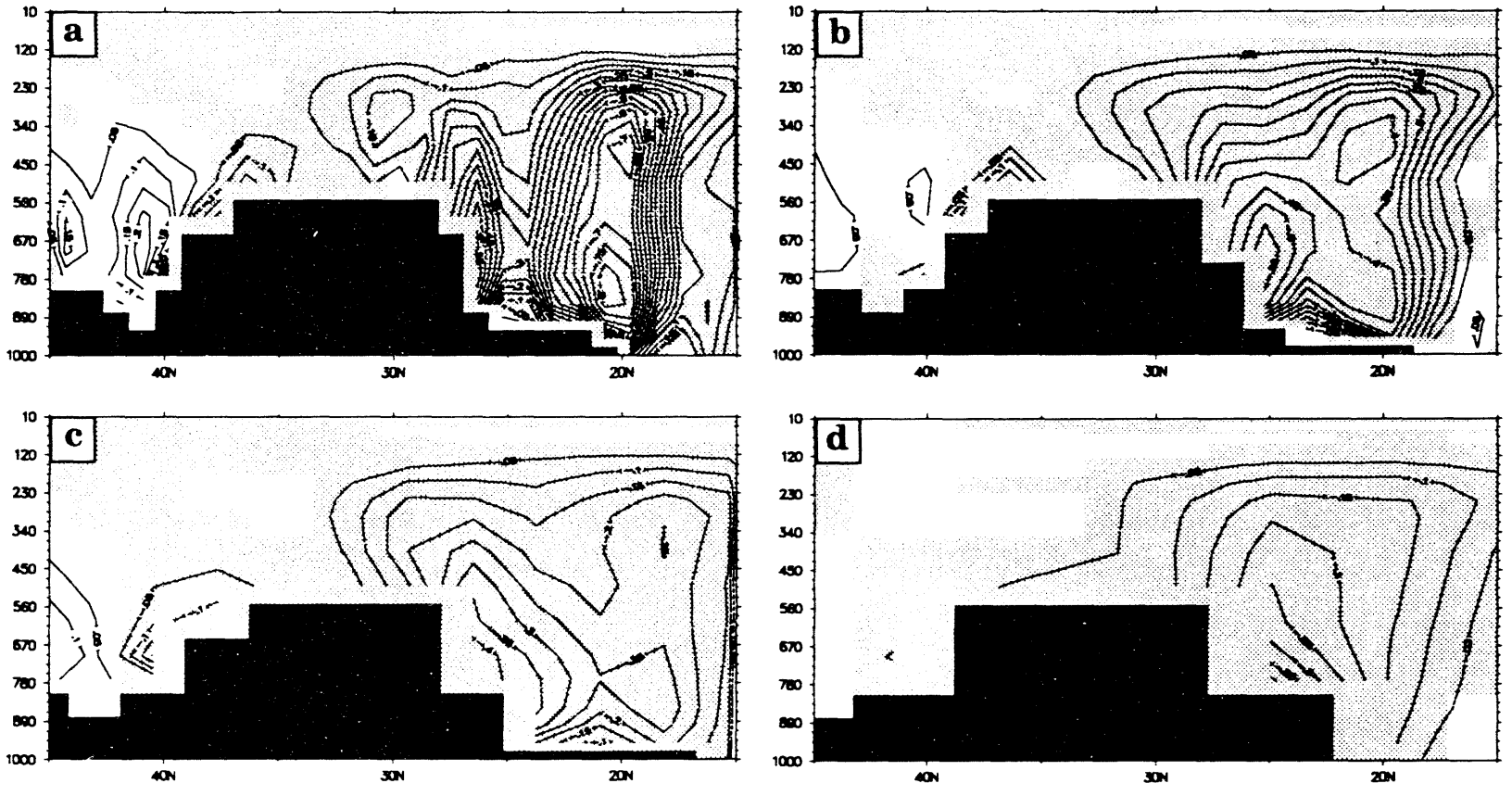

Figure 11. June cross-section vertical velocity (Pa s^{-1}) near 92°E a) T106, b) T63, c) T42, and d) T21. Light shading denotes ascent and black corresponds to topography.

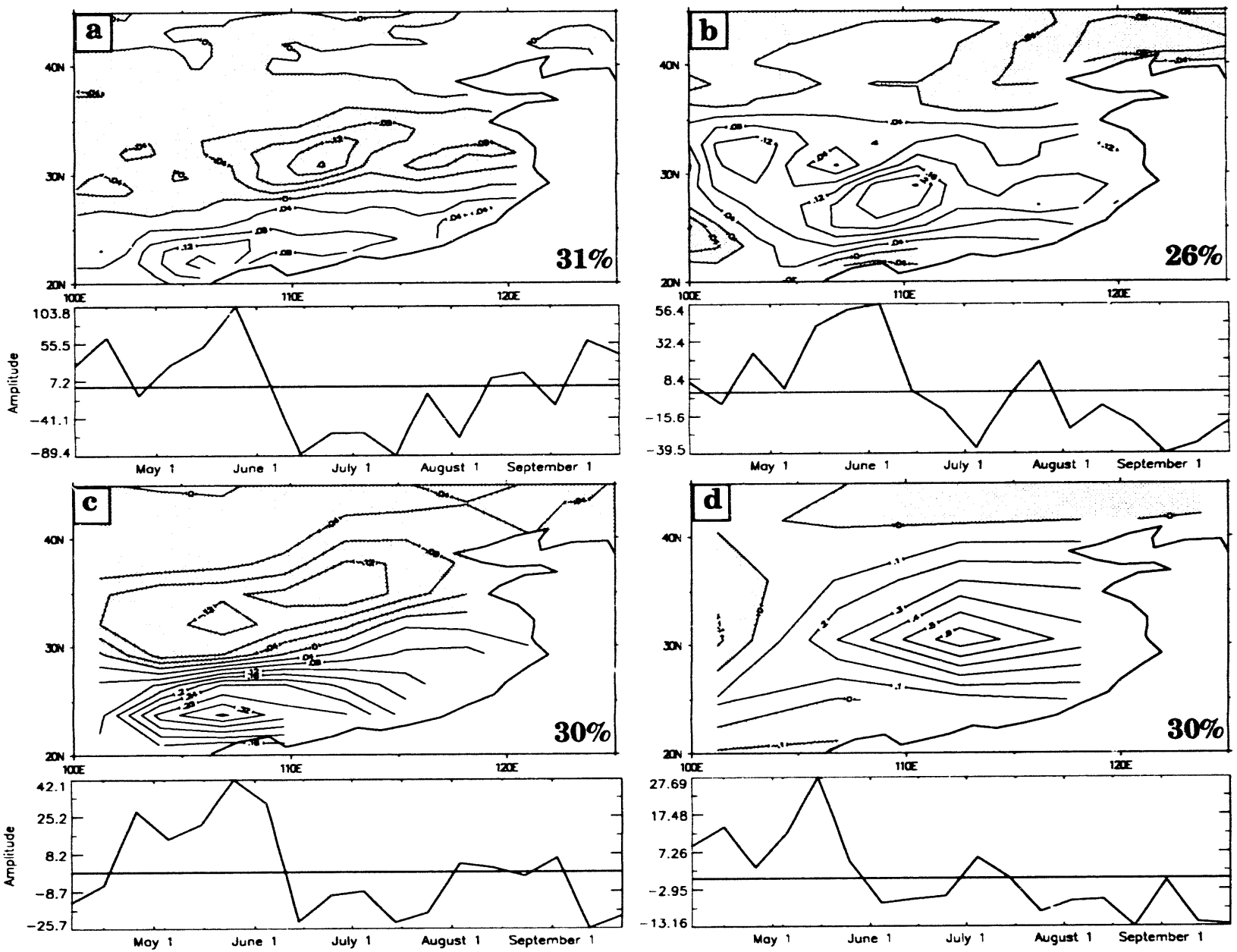

Figure 12. First eigenvector and principal component time series over China for the period April-September (10-day means) a) T106, b) T63, c) T42, and d) T21. This EOF/PC corresponds to the seasonal cycle. Negative spatial loading is shaded.

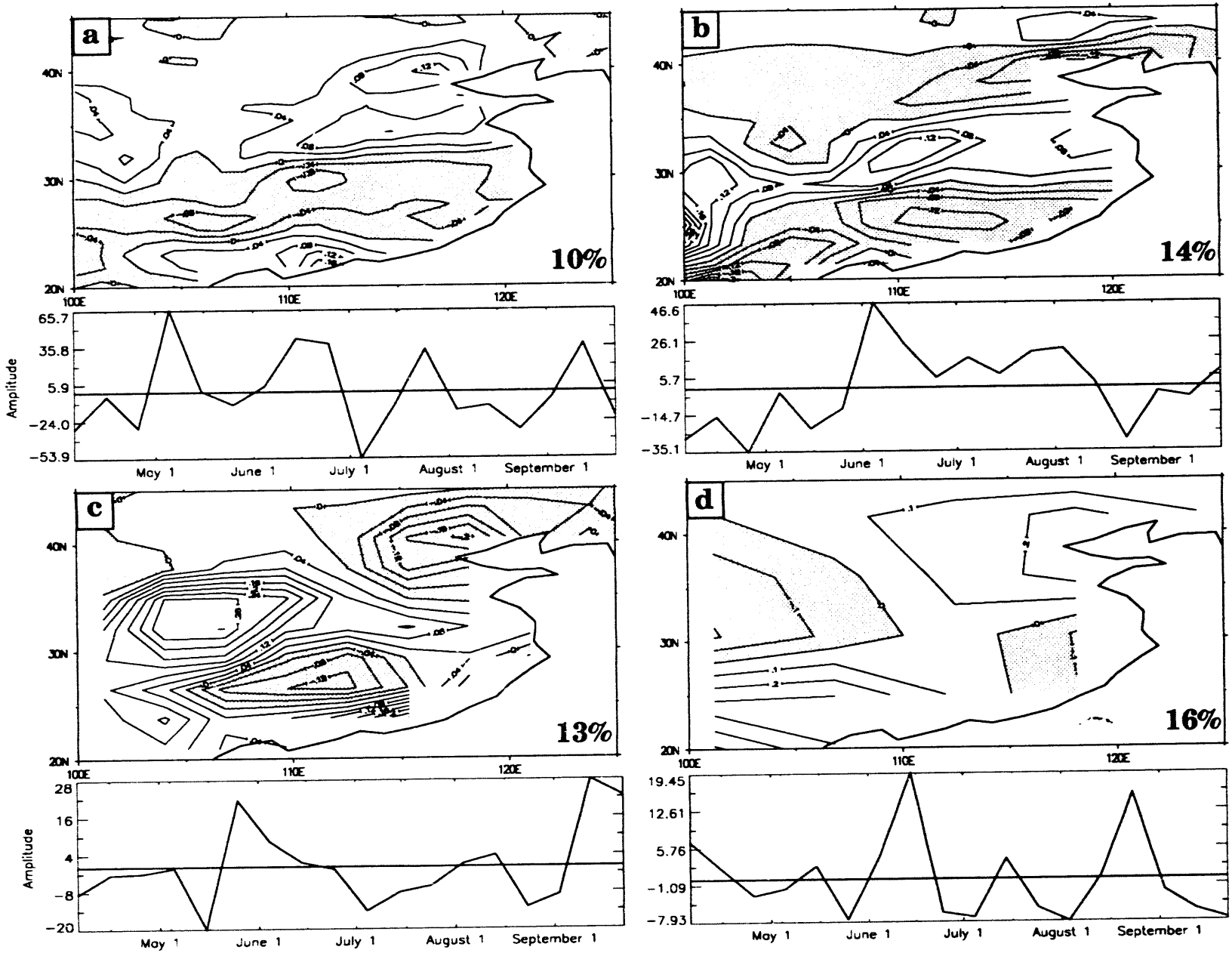

Figure 13. Third eigenvector and principal component time series over China for the period April-September (10-day means) a) T106 b) T63 c) T42 d) T21. This EOF/PC corresponds to the dominant Mei-yu mode. Negative spatial loading is shaded.

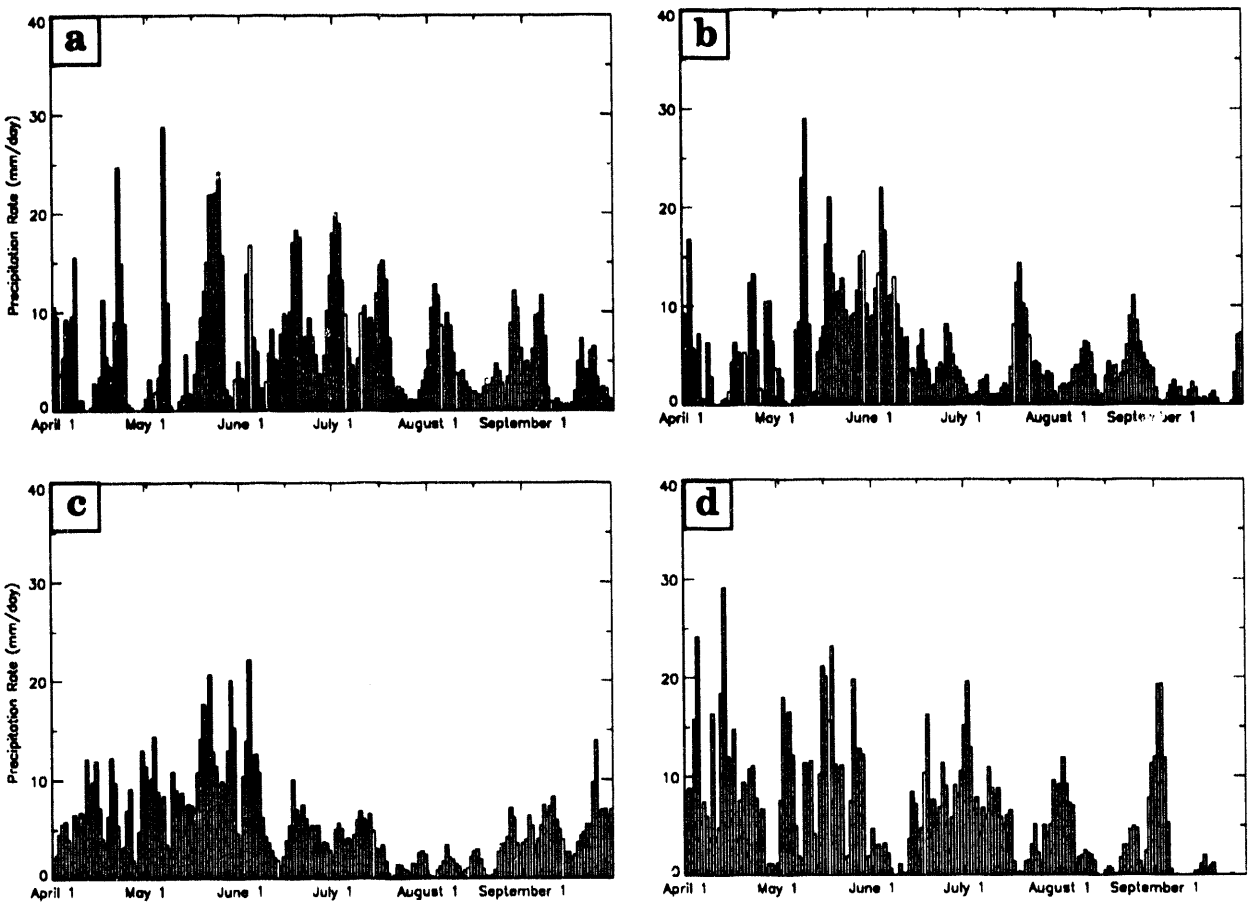

Figure 14. Daily precipitation (mm) averaged over the Yangtze River Valley (grid points that are encompassed by 110°E-125°E, 25°N-32.5°N) a) T106, b) T63, c) T42, and d) T21.

PCMDI REPORTS

Number	Title	Authors(s)	Date
1	The Validation of Atmospheric Model	W. L. Gates	March 1992
2	Analysis of the Temporal Behavior of Tropical Convection in the ECMWF Model	J. M. Slingo K. R. Sperber J.-J. Morcrette G. L. Potter	April 1992
3	The Effect of Horizontal Resolution on Ocean Surface Heat Fluxes in the ECMWF Model	P. J. Gleckler K. E. Taylor	July 1992
4	Behavior of an Ocean General Circulation Model at Four Different Horizontal Resolutions	C. Covey	August 1992
5	The Effects of Sampling Frequency on the Climate Statistics of the ECMWF General Circulation Model	T. J. Phillips W. L. Gates K. Arpe	September 1992
6	Sensitivity of Dynamical Quantities to Horizontal Resolution in a Climate Simulation with the ECMWF Atmospheric General Circulation Model (Cycle 33)	J. S. Boyle	October 1992
7	AMIP: The Atmospheric Model Intercomparison Project	W. L. Gates	December 1992
8	The Impact of Horizontal Resolution on Moist Processes in the ECMWF Model	T. J. Phillips L. C. Corsetti S. L. Grotch	January 1993

Number	Title	Authors(s)	Date
9	A Modeling Perspective on Cloud Radiative Forcing	G. L. Potter J. M. Slingo J.-J. Morcrette L. Corsetti	February 1993
10	The Use of General Circulation Models in Detecting Climate Change Induced By Greenhouse Gases	B. D. Santer U. Cubasch U. Mikolajewicz G. Hegerl	March 1993
11	Preliminary Validation of the Low Frequency Variability of Tropospheric Temperature and Circulation Simulated for the AMIP by the ECMWF Model	J. S. Boyle	April 1993

DATE
FILMED
2/2/94
END